Microsyst Technol (2017) 23:23–37
DOI 10.1007/s00542-015-2695-0

TECHNICAL PAPER

The analysis of internal transient flow and the performance of valveless piezoelectric micropumps with planar diffuser/nozzles elements

Xiuhua He[1] · Jiawei Zhu[1] · Xitong Zhang[1] · Liang Xu[1] · Song Yang[2]

Received: 24 June 2015 / Accepted: 29 September 2015 / Published online: 19 October 2015

Abstract The influences of diverging angle, excitation frequency and volume change rate of the pump chamber on the valveless piezoelectric micropump with planar diffuser/nozzle elements are studied. The diverging angle ranges from 5° to 60°, the amplitude of the membrane ranges from 0.5 to 80 μm, the excitation frequency ranges from 10 to 5000 Hz. The deformation model of the membrane is verified by experiments. The performance of the micropump is predicted by numerical simulation. The simulation results agree with the experiment results very well. Statistical analysis of the location and duration of vortexes in internal flow field is used to reveal the relationships among efficiency, diverging angle, frequency and chamber volume change rate. As the frequency ranges from 100 to 1000 Hz, the efficiency increases sharply because the tube is partially blocked by vortexes at suction stage. The vortexes in the diffuser/nozzle elements is brought by the great adverse pressure gradient at the high frequency.

List of symbols

a	The radius of the central part
b	The outer radius of the outer region
f	Excitation frequency
H	The deep of the diffuser/nozzle element
L	The length of the diffuser/nozzle element
P_{in}	The pressure at the inlet
P_{out}	The pressure at the outlet
$q(t)$	Transient flow rare
R	The rounding at the throat
T	Period
$\bar{v}$	The average velocity at the throat
V	The volume change of the pump chamber
w_1	The deflection of the central part
w_2	The deflection of the outer region
$w_{\max}$	The amplitude of the membrane
W	The width of the throat
θ	Diverging angle
ρ	Density of the medium
η	Efficiency of the piezoelectric micropump

1 Introduction

Micropump is the core component of the Micro-fluidics-system. It can be classified into two categories: the mechanical micropumps and the non-mechanical micropumps by their pumping mechanisms (Singhal and Garimella 2004). The mechanical micropumps use a moving part to transport the fluid such as rotary pumps, vibrating diaphragm pumps, and peristaltic pumps (Ahn and Allen 1995; Dewa and Deng 1997; Hsu and Le 2009).

✉ Xiuhua He
xiuhua.he@ujs.edu.cn

Jiawei Zhu
zhujiawei_ujs@sina.com

Xitong Zhang
zhangxitong_ujs@sina.com

Liang Xu
edward_anglo@126.com

Song Yang
yangmiaohao@126.com

[1] School of Energy and Power Engineering, Jiangsu University, No. 301, Xuefu Road, Zhenjiang 212013, Jiangsu Province, People's Republic of China

[2] Hydraulic Machine Center, Jiangsu University, No. 301, Xuefu Road, Zhenjiang 212013, Jiangsu Province, People's Republic of China

Non-mechanical micropumps have no moving parts and drive the fluid directly by the electric, magnetic, thermal, chemical and acoustic energy. In terms of this, electrokinetic micropumps, magnetokinetic micropumps, phase change micropumps (Lu and Xie 2005; Wang and Cheng 2009; Kuo and Liu 2009; Su and Chen 2006; Aravind and Kumar 2013; Cheng and Wu 2007) and other novel micropumps are categorized as non-mechanical micropumps. The piezoelectric micropump is a kind of vibrating diaphragm pumps, which has the great advantages of small size, low power consumption, no electromagnetic interference and insensitivity of fluid density, ionic strength, acidity and basicity. In addition, the piezoelectric micropump could pump the fluids successfully within a wide viscosity range (Andersson and Wijngaart 2001). Benefited from these outstanding performance above, the piezoelectric micropump developed rapidly in the past decades.

Again, by mechanism, the piezoelectric micropump can be classified as piezoelectric micropumps with valves and valveless piezoelectric micropumps. The first piezoelectric micropump with valves is fabricated by W.J. Spencer at Sandia National Laboratory in 1978 (Spencer 1978). This kind of micropump has the advantages of high efficiency and great output pressure (Bodén 2006). However, moving parts are prone to wear and difficult to manufacture. Besides, the movement of the passive valve and the volume change of the pump chamber are out of sync at high excitation frequency (Tanaka and Tsukamoto 2008). The mechanism of valveless piezoelectric micropump is based on the flow characteristics in the special tubes and avoid the disadvantages of the piezoelectric micropumps with valves. The valveless piezoelectric micropumps are simple structure, easy fabrication (Wang and Hsu 2009), better performance at high excitation frequency (Stemme and Stemme 1993; Olsson et al. 1995; Nguyen et al. 2002) and more suitable for miniaturization and integration. There are various special tubes in valveless micropumps, such as diffuser/nozzles, Tesla tubes, saw-tooth tubes, V-shape tubes, three-way diffuser/nozzle elements, R-NMP microvalves (Wang and Chen 2014; Guan et al. 2009; Yuan and Yang 2015; Izzo et al. 2007) and so on. Valveless piezoelectric micropumps with diffuser/nozzle elements are studied widely.

Jiang and Zhou (1998) investigate the valveless piezoelectric micropumps. They discovery that the performance of the micropumps relies on the tube parameters and Reynolds numbers. The diverging flow coefficient, the converging flow coefficient and the flow coefficient ratio of nozzle to diffuser all decrease with an increase in diverging angles which range from 5° to 10°. The net flow direction is determined by the flow coefficient ratio. Olsson and Stemme (2000) find that the net flow direction depends on diverging angle but not the length. And the experiments results agree well with the simulations results at low Reynolds numbers. Singhal et al. (2004) present the relationships between the pressure loss coefficient and diverging angles. The results show that the pressure loss coefficients for low Reynolds number laminar flows are a strong function of the flow Reynolds number, especially, at small diffuser angles. The variation of pressure loss coefficient with Reynolds number follows opposite trends for small and large diffuser angles. In 2005, valveless piezoelectric micropump is used to improve the performance of the direct methanol fuel cell by Zhang and Wang (2005). The relationships of current density and net power output at different excitation frequency and flow rate are given. A larger excitation frequency could decrease the power consumption of the micropump. Wang and Hsu (2009) make an intensive study of pressure loss coefficient in diffuser/nozzle elements as the diverging angles range from 4° to 120° and the Reynolds numbers range from 100 to 2000. They find that the optimal angle is 40° when the Reynolds number is 100; the optimal angle is 20° when the Reynolds number is larger than 500. He and Cai (2014) employ the commercial software CFX to study the transient flow characteristics in planar diffuser/nozzles element. The investigation is reported as the diverging angles are 5° and 10° at different frequency numbers. They discovery that the flow resistance coefficients increase with an increase in frequency. The net flow through the tubes cuts down while the duration of vortexes increases.

In valveless micropump, the efficiency is defined as the ratio of the net flow and the volume change of the pump chamber in a cycle (Singhal et al. 2004). The efficiency of diffuser/nozzle micropumps reported in the literature is very low, generally between 0.01 and 0.2. Hence, it is important to improve the efficiency by means of further study.

The previous researches indicate that the efficiency of the valveless micropumps with diffuser/nozzle elements is determined by the parameters of the diffuser/nozzles, the excitation frequency and the Reynolds numbers. Nevertheless, the effect of the frequency is paid little attention to. In this paper, the displacement of the membrane is studied by experiment firstly. And then, the influences of the diverging angle, excitation frequency and volume change rate of the pump chamber on the efficiency are presented. The relationships among the influence factors, the vortex characteristics and the efficiency of micropumps are discussed by the statistical analysis of the location and duration of the vortexes in internal flow field. The analyses of the distributions of the pressure in outlet tubes are applied as supplementary explanations.

2 Operation principle

The piezoelectric membrane is employed as the driving device in the valveless piezoelectric micropump with planar diffuser/nozzle elements. The two planar diffuser/nozzle elements have the same divergence. When an alternative voltage is applied on the membrane, the working stages are shown as Fig. 1. The membrane moves from the solid lines to the dashed lines.

In Fig. 1a, d, as the volume of the pump chamber increases, the fluid is sucked into the pump chamber. According to the acceleration of the membrane, the two stages are named as acceleration suction stage and deceleration suction stage, respectively. The inlet flow rate is larger than the outlet flow rate as the flow resistance in diverging direction is smaller than that in converging direction at small diverging angles (Singhal et al. 2004). In Fig. 1b, c, as the volume of the pump chamber decreases, the fluid is discharged from the pump chamber. The flow rate through the outlet tube is larger than that through the inlet tube. The two stages are named as acceleration pump stage and deceleration pump stage, respectively.

The mean flow rate through the tubes at the suction stage could be written as

$$Q_{\mathrm{s}} = \frac{2}{T}\left[\int_0^{T/4} q(t)dt + \int_{3T/4}^{T} q(t)dt\right] \tag{1}$$

The mean flow rate through the tubes at the pump stage could be written as

$$Q_{\mathrm{p}} = \frac{2}{T}\int_{T/4}^{3T/4} q(t)dt \tag{2}$$

where $q(t)$ is the transient flow rate, Q is the flow rate, the subscript s denotes the suction stage and p denotes the pump stage, T is the time of a cycle.

The fluid is assumed incompressible as the variation of the pressure in the chamber is not great. And the net flow rate Q_{net} could be described as follow

$$\begin{aligned} Q_{\mathrm{net}} &= \left(Q_{\mathrm{inlet,s}} + Q_{\mathrm{inlet,p}}\right)/2 = \left(Q_{\mathrm{outlet,p}} + Q_{\mathrm{outlet,s}}\right)/2 \\ &= \frac{1}{T}\int_0^T q(t)dt \end{aligned} \tag{3}$$

where Q_{inlet} and Q_{outlet} denote the mean flow rate through the inlet tube and the outlet tube, respectively.

3 Experiments

3.1 Experimental setup

The piezoelectric micropump is fabricated by MEMS technology. The diffuser/nozzle elements and chamber on the silicon wafer are fabricated by deep reactive ion etching and sealed with a glass wafer bonded to the silicon wafer. The piezoelectric vibrator is composed of the piezoelectric ceramic (PZT), the binder and the membrane (copper). Figure 2 shows the exploded view of the micropump. The width of the throat (the minimum width of the diffuser/

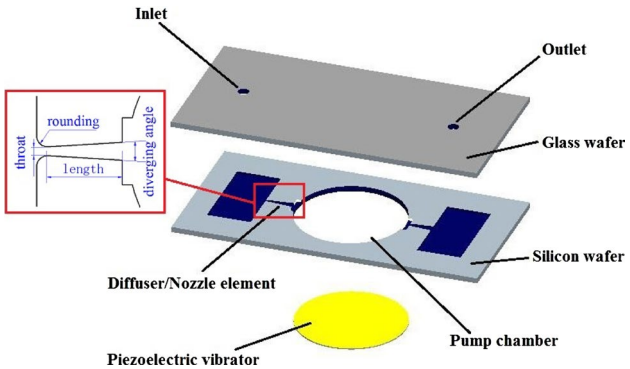

Fig. 2 The exploded view of the piezoelectric micropump

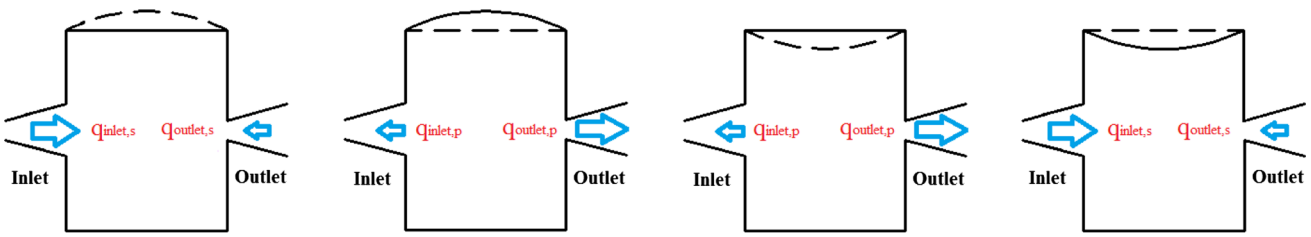

Fig. 1 The schematic of working stages

nozzle element) is 150 μm. The length and depth of the diffuser/nozzle element are 3 mm and 150 μm, respectively. The rounding at the throat is 75 μm. The diverging angle is 7° and the diameter of the pump chamber is 10 mm.

The schematic and photo of the experimental apparatus are shown in Fig. 3. The piezoelectric micropump is driven by a series of sinusoidal voltage with different frequencies. The voltage is provided by the function generator (Tektronix, AFG3022B) and amplified by a power amplifier (Fo Neng, HVP-300A). The excitation voltage is monitored by oscilloscope (Tektronix, TBS1022). The scanning vibrometer (polytec MSA-500) is employed to measure the membrane displacement. The flow rate of the micropump is obtained by measuring the mass of fluid transported in 5 min by using an electronic balance (Jiming, JM-A). The medium is distilled water. In order to improve the filling of the chamber with water, the system is well primed continuously with 99 % Ethanol to clean the chamber and remove air, initially.

4 Simulations

4.1 Structure parameters and boundary conditions

The schematic of the structure and computational domain are shown as Fig. 4. The minimum width *W* of the diffuser/nozzle element is 100 μm; the ratio of the length and width

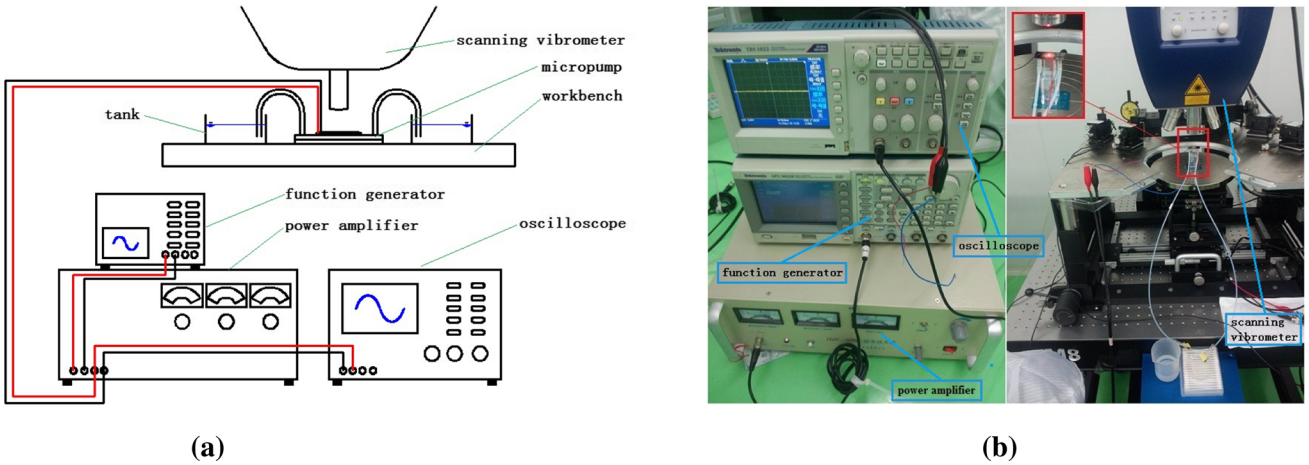

Fig. 3 The schematic and photo of the experimental apparatus

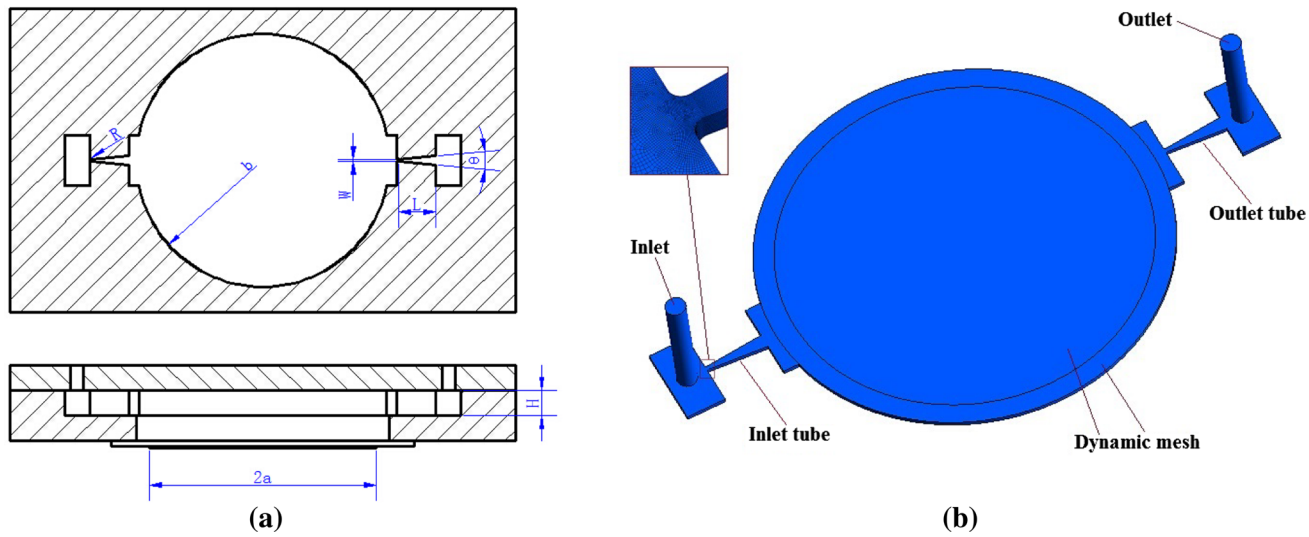

Fig. 4 **a** The schematic of structure, **b** computational domain

Table 1 The volume change rate under different $w_{max} \times f$

$w_{max} \times f$/μm s^{-1}	The volume change rate/ml s^{-1}
500	0.071
550	0.078
600	0.085
700	0.099
800	0.113

is 15 (Wang and Hsu 2009); the depth H is 100 μm; the rounding R is 50 μm; the diverging angles θ range from 5° to 60°; the radius of the piezoelectric disk a is 4.5 mm; the radius of the membrane b is 5 mm.

The deformation model of the membrane proposed by Bu et al. (2003) is employed. In Bu's method, the membrane is divided into two sections: the central part (a bimorph) of radius a and the outer region (an annulus with inner radius of a and outer radius of b). The thickness of the binder is neglected for its thin thickness. When a sinusoidal excitation voltage is applied to the PZT disc, the deflection of the central part $w_1(r)$ and the outer region $w_2(r)$ are given by Eqs. (4), (5) (Yang et al. 2014):

$$w_1(r) = w_{\max}\left(1 + \frac{b^2r^2 - a^2r^2}{2a^2b^2\mathrm{In}\frac{a}{b}}\right)\sin(2\pi ft), \quad (0 \le r \le a) \tag{4}$$

$$w_2(r) = w_{\max}\left(\frac{b^2 + 2b^2\mathrm{In}\frac{r}{b} - r^2}{2b^2\mathrm{In}\frac{a}{b}}\right)\sin(2\pi ft), \quad (a \le r \le b) \tag{5}$$

where $w_{\max}$ is the amplitude of the center of the membrane; f is the excitation frequency; t is the time.

The time-varying geometry of the dynamic mesh is given by Eqs. (4), (5). The volume change rate (volume change per second) of the pump chamber depends on $w_{\max}$ and f. In order to analyze the influence of $w_{\max}$ and f, independently, an assumption is proposed that the volume change rate is fixed. The relationships between $w_{\max} \times f$ and the volume change rate are shown in Table 1.

Table 3 Time step independence for 7° diffuser at f = 100 Hz

Time step/s	Flow rate/ml min^{-1}	Relative error/%
1/(50f)	0.539	0.73
1/(100f)	0.536	0.17
1/(200f)	0.536	0.08
1/(400f)	0.535	–

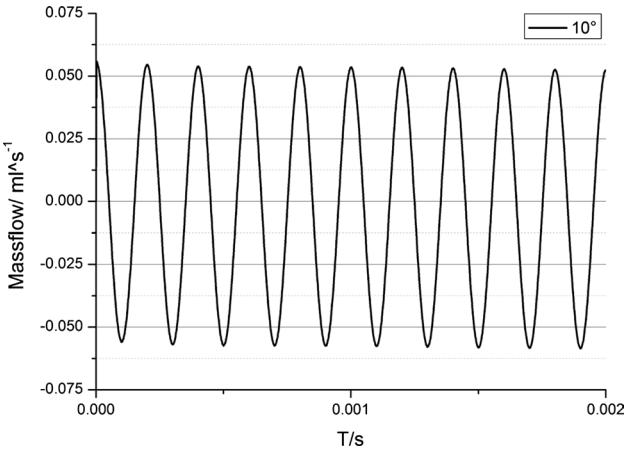

Fig. 5 The flow rate of the outlet tube in ten cycles as the excitation frequency is 5000 Hz and $\theta = 10°$

The working medium is water, which temperature is 25 °C, the density is 1.01 × 10^3 kg/m^3 and the kinematic viscosity is 1 × 10^{-6} m^2/s. No-slip conditions are applied to the walls; the ambient pressure is the atmospheric pressure; the initial state is motionless. The SST model (Shear-Stress Transport κ-ω model) is used in the simulation because of the high accurate prediction of flows with strong adverse pressure gradients and separation (Menter et al. 2003).

The grid and time step sensitivity studies are carried out and the results are shown in Tables 2 and 3, respectively. All errors are calculated relative to the data from the finest one. The number of 2,088,660 elements is enough for the simulation. So, the number of the grid ranging from 2,088,660 to 2,798,080 is reasonable. The influence of time

Table 2 Grid independence for 7° diffuser at f = 100 Hz

Mesh at diffuser neck (W × H)	Total grid number	Flow rate/ml min^{-1}	Relative error/%
10 × 10	332,545	0.544	7.10
20 × 10	468,670	0.544	7.15
20 × 20	954,060	0.536	5.51
30 × 20	1,520,440	0.524	3.12
30 × 30	2,088,660	0.511	0.64
30 × 40	2,798,080	0.508	–

step is not conspicuous. The relative error is only 0.73 % when the time step is 1/(50*f*). The time step setting at 1/(100*f*) is suitable.

As Fig. 5 shown, the transient flow rate is tended to be stable gradually until the eighth cycle (the relative difference of the mean flow rate between the current cycle and the next cycle is less than 1 %). Therefore, when the excitation frequency is less than 200 Hz, the number of cycles is set at two; when excitation frequency ranges from 200 to 1000 Hz, the number of cycles is set at three; when excitation frequency is larger than 1000 Hz, the number of cycles is set at ten.

5 Results and analysis

5.1 Experimental results and discussion

The profile of the membrane is investigated as the voltage is 150 V_{p-p} and the frequency is 100 Hz. The center point of the membrane is set as the origin of coordinate. The displacement of the membrane is measured along the radius and the results are shown in Fig. 6. The amplitude of the center point is 8.44 μm. The results calculated by Eqs. (4), (5) agree well with the experimental results. The relative errors are less than 5 % as radius ranges from 0 to 3.5 mm. However, the relative error is 17.3 and 18 % as the radius is 4 and 4.5 mm, respectively. The accuracy of Bu's model is not very good at the common boundary of the central part and the outer region. In spite of this, the model is still suitable.

The responses of w_{max} to the voltage are studied when the frequency is 100 Hz. The step of voltage is 25 V_{p-p}. The results are displayed in Fig. 7. The relationship between

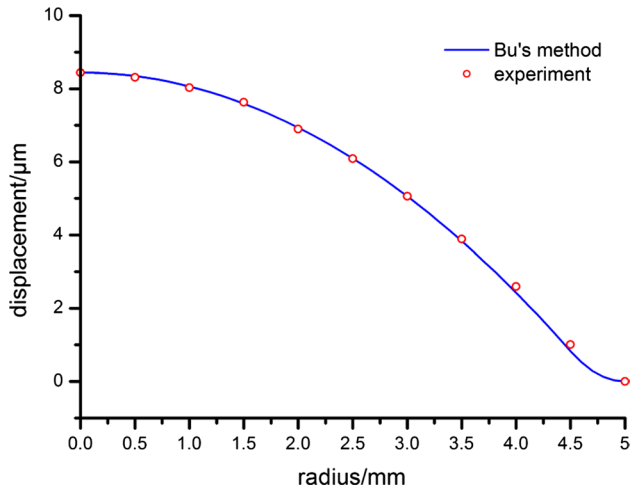

Fig. 6 The profile of the membrane when the voltage is 150 V_{p-p} and the frequency is 100 Hz

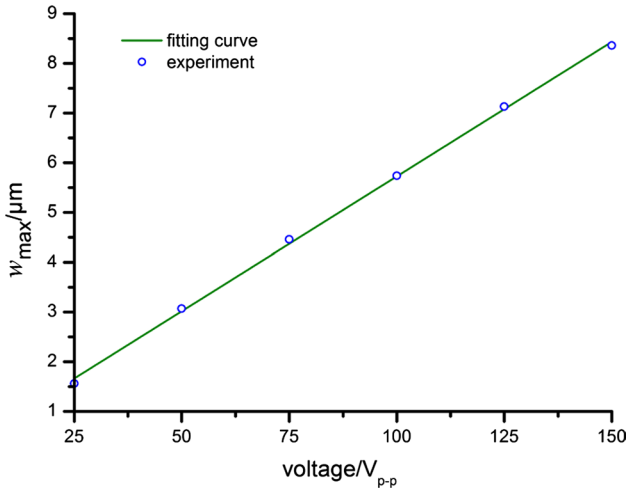

Fig. 7 The responses of w_{max} to the voltage

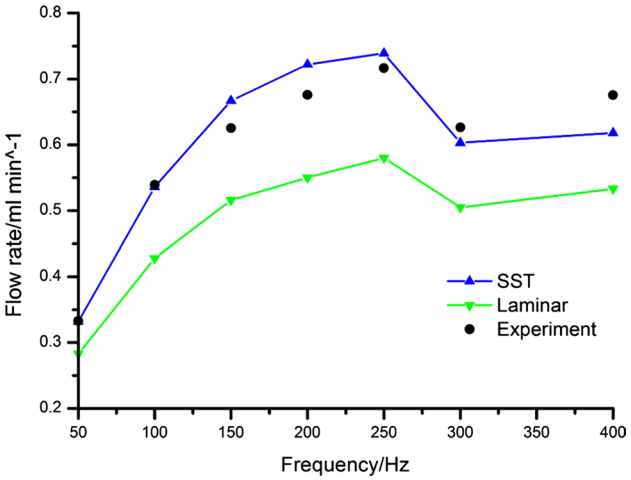

Fig. 8 The comparison of the experiments and simulations

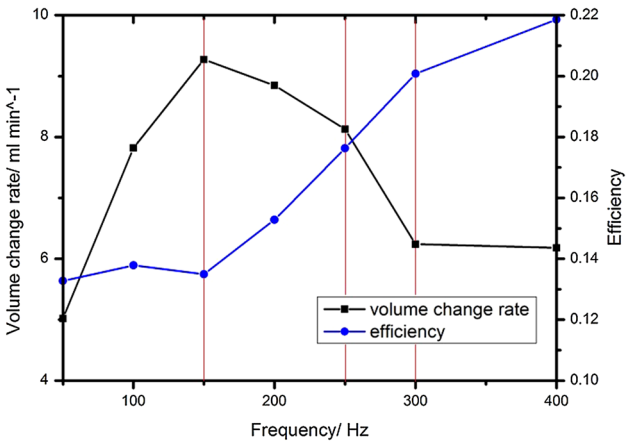

Fig. 9 The volume change rate and the efficiency in the experiments

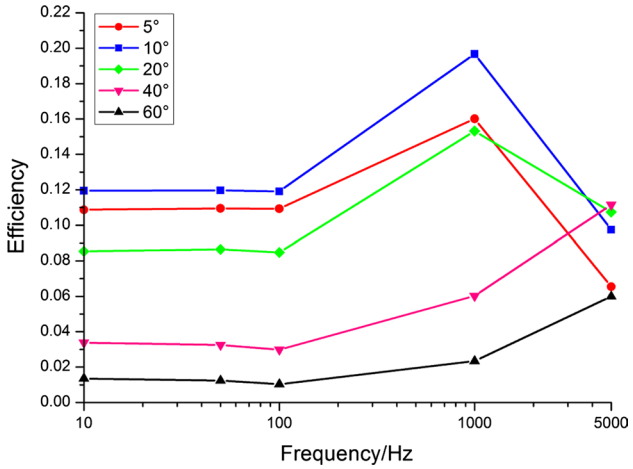

Fig. 10 The efficiency under different diverging angles and frequencies when $w_{max} \times f = 500$

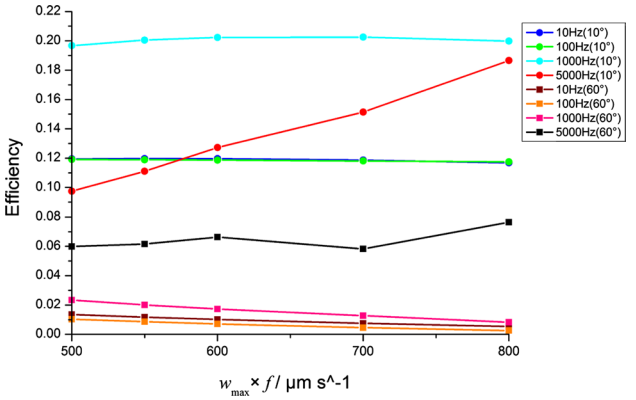

Fig. 11 The efficiency under different frequencies and $w_{max} \times f$ when diverging angles are 10° and 60°

w_{max} and voltage is linear. That means the volume change rate increases linearly with an increase in voltage.

The flow rate of the micropump is measured when the voltage is 150 V_{p-p} and the frequency ranges from 50 to 400 Hz. The numerical simulations are used to predict the performance of the micropump. In these cases, the SST mode and the laminar mode are employed. The comparison of the experiment results and simulation results are shown in Fig. 8. Obviously, the results of SST mode coincide with the experiments better than those of laminar mode. The maximum relative error against the results of SST mode and experiment is 8.5 %. The maximum Reynolds numbers of these cases range from 700 to 1200. The assumption of turbulent flow is more reasonable. The conclusion agree with Gravesen's (Gravesen and Branebjerg 1993) and Peng's (Peng et al. 1994).

The flow rate depends on the volume change rate and efficiency. As shown in Fig. 9, the volume change rate is variable. And the efficiency increases as an increase in frequency. As the frequency is less than 150 Hz, the volume change rate increases sharply with an increase in frequency. The flow rate increases. As the frequency ranges from 150 to 250 Hz, the volume change rate decreases slightly with an increase in frequency. The flow rate still increases due to an increase in efficiency. However, as the frequency ranges from 250 to 300 Hz, the volume change rate decreases sharply with an increase in frequency. And the flow rate decreases. Similarly, it is easy to explain the increase of flow rate as the frequency is larger than 300 Hz. If the influence of volume change rate on the efficiency is neglected, the trend of efficiency in the experiments corresponds to the simulations (refer to Fig. 10).

5.2 Simulation results and analysis

The efficiency of the valveless piezoelectric micropump with diffuser/nozzle elements is defined as the ratio of the net flow and the volume change of the pump chamber in a cycle

$$\eta = \frac{\int_0^T q_{in} dt}{V} = \frac{\int_0^T q_{out} dt}{V} \tag{6}$$

where q is the transient flow rate, V is the volume change.

The efficiency of the micropump is presented in Fig. 10 as the diverging angle ranges from 5° to 60° and the frequency ranges from 10 to 5000 Hz. The optimal diverging angle is 10° as $f \leq 1000$ Hz. In addition, the efficiency decreases with an increase in diverging angle as $\theta \geq 20°$. The excitation frequency has no significant effect on the efficiency when $f \leq 100$ Hz. The efficiency of each micropumps increases with a rise in excitation frequency as the frequency ranges from 100 to 1000 Hz and the maximum increment is 7.77 % when the diverging angle is 10°. Then, the efficiency decreases with an increase in frequency as the frequency is larger than 1000 Hz. The efficiency decreases by 59.2, 50.5 and 29.9 % when $\theta = 5°$, 10° and 20°, respectively. On the contrary, the efficiency increases by 85.3 and 156 % when $\theta = 40°$, 60°, respectively. Besides, the maximum efficiency reaches 19.67 % when $\theta = 10°$ and $f = 1000$ Hz.

The efficiency of the micropumps at 10° and 60° is shown in Fig. 11 as $w_{max} \times f$ ranges from 500 to 800. Although the net flow rate increases with an increase in volume change rate (Azarbadegan and Eames 2011), the efficiency decreases at a wide range of frequency except that frequency is 5000 Hz.

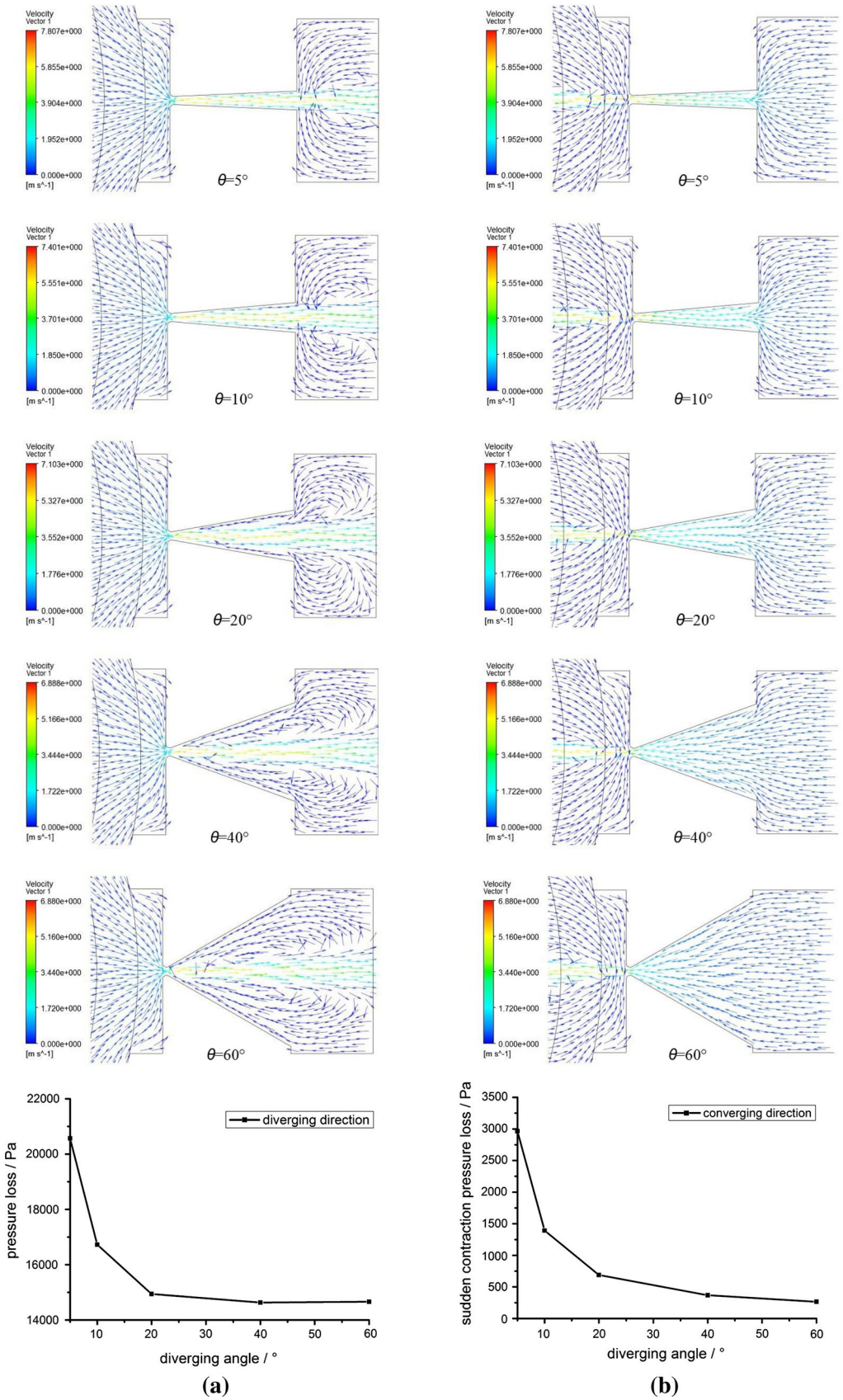

Fig. 12 The distributions of the velocity and the pressure loss in the tubes with different diverging angles as the frequency is 10 Hz. **a** $t = 0.4T$. **b** $t = 0.9T$

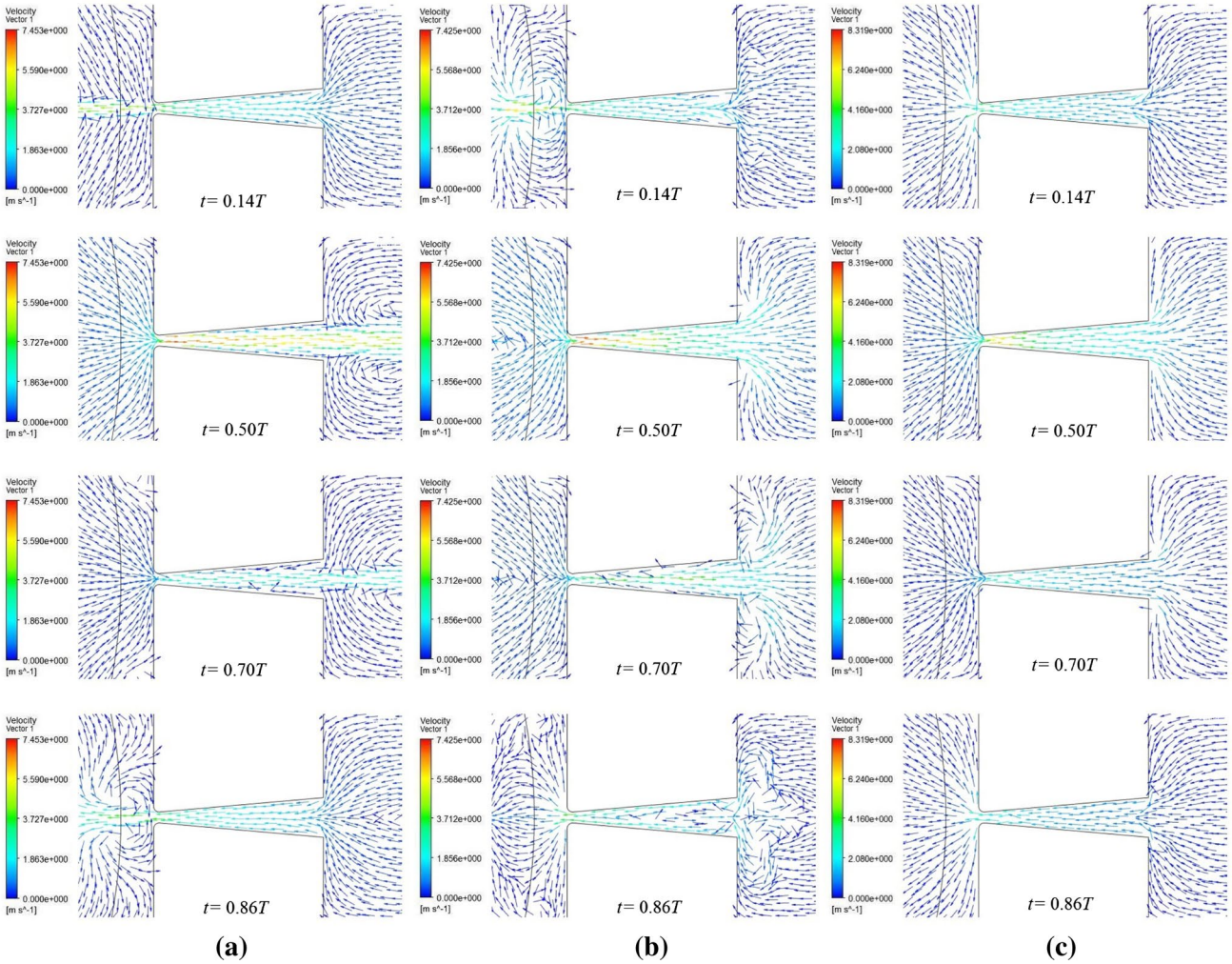

Fig. 13 The distribution of the velocity in the outlet tube in a cycle under different frequency. **a** $f = 100$ Hz. **b** $f = 1000$ Hz, **c** $f = 5000$ Hz

5.2.1 The influence of the diverging angles on efficiency

The distributions of the velocity and the pressure loss in the outlet tubes are shown in Fig. 12 as the diverging angles range from 5° to 60° and the frequency is 10 Hz. As $\theta \leq 10°$, no boundary layer separation occurs. As the diverging angle increases, the pressure loss (the difference in pressure between the left side of the buff chamber and the outlet, refer to Fig. 19) in the diverging direction decreases rapidly because of pressure recovery (the phenomenon of an increase in pressure in diverging flow due to the transformation of kinetic energy to pressure energy). As $\theta \geq 20°$, the boundary layer separation appears and the diverging flow is independent of the diverging angles. The flow regime is jet flow. There are two vortexes on both sides of the mainstream. With an increase in diverging angles, the effective diffusion region (the region within the boundary of the jet flow in the tubes) of the fluid is almost invariant; the pressure loss is almost invariant identically. In Fig. 12b, the distributions of the velocity are similar in different angels as the fluid flows in the contraction direction. No boundary layer separation occurs in the tubes. The pressure loss depends on the pressure loss of sudden contraction. Consequently, as $\theta \leq 10°$, the efficiency is determined by the diverging flow because of the effective diffusion region; as $\theta \geq 20°$, the efficiency is determined by the converging flow because of the sudden contraction pressure loss.

5.2.2 The influence of the excitation frequency on efficiency

As the frequency ranges from 100 to 5000 Hz and $\theta = 10°$, the distributions of the velocity in the outlet tube are shown in Fig. 13, the start of the boundary layer separation and the disappearance of the vortexes in the outlet

Table 4 The start of the boundary layer separation and the disappearance of the vortexes in the outlet tube as $\theta = 10°$

Frequency/Hz	Boundary layer separation inception/T	The disappearance of the vortexes/T
10	–	–
50	0.68T	0.78T
100	0.58T	0.80T
1000	0.62T	0.98T
5000	0.70T	0.85T

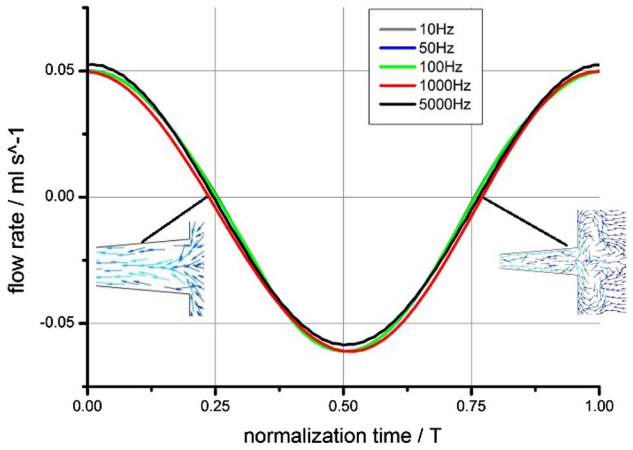

Fig. 14 The flow rate of the outlet tube as the frequency ranges from 10 to 5000 Hz and $\theta = 10°$

tube are shown in Table 4 and the flow rates are shown in Fig. 14. As $f \leq 100$ Hz, the flow regimes are similar, the flow rate curves almost overlap. The boundary layer separation occurs at the end of the tubes in the deceleration pump stage. The effective diffusion region and the efficiency decrease slightly with an increase in the frequency. As $f = 1000$ Hz, during the deceleration suction stage, the vortexes at the end of the tube expand as time goes on. In this process, the tube is partially blocked and the flow rate decreases in contraction direction, the deceleration suction stage ends in advance. At the acceleration pump stage, the flow regime is similar to the flow regimes as $f \leq 100$ Hz. During the deceleration pump stage, the boundary layer separation appears in the middle of the tube. With the process goes on, the region of the boundary layer separation extend to the throat and the end of the tube, the effective diffusion region decreases. The vortexes caused by the boundary layer separation would not disappear until the end of the acceleration suction stage. The start of the acceleration suction stage delays, the tube is partially blocked by the vortex at the suction stage and the flow resistance in the contraction direction increases relatively, the efficiency increases. As $f = 5000$ Hz, the flow regimes at the first two stages are similar to the flow regimes at $f \leq 100$ Hz. The boundary layer separation appears after 0.7 T. The vortexes have little time to gain energy and disappear rapidly at the acceleration suction stage. The effect of blocking is slight. Hence, the efficiency is smaller than that at 1000 Hz.

The distributions of the velocity in the outlet tube under different diverging angels as $f = 1000$ Hz and $t = 0.86T$ are shown in Fig. 15. The tubes are partially blocked by the vortexes in contraction direction. The effects of vortexes are more significant in small diverging angle tubes. With an increase in diverging angles, the flow region increases, the effect of blocking decreases. Consequently, the amplification of the efficiency decreases with an increase in diverging angles. However, as $\theta = 5°$, the appearance of the boundary layer separation is too late. The vortexes have little time to gain energy. The duration of the vortexes is just 0.15 T at the acceleration suction stage. As the vortexes disappear, the fluid is sucked into the pump chamber normally, so the amplification of the efficiency is smaller than that case with $\theta = 10°$.

In Fig. 16, as $f = 5000$ Hz, the boundary layer separation appears at 0.58 T and 0.55 T, when $\theta = 40°$ and $\theta = 60°$, respectively. The vortexes disappear until the end of the acceleration suction stage. The tubes are blocked partially. As $f = 1000$ Hz, the vortexes are located in the middle/end of the tube at the acceleration suction stage. The effects of the vortexes are not really great because the widths at the end of the tubes are wide enough. Nevertheless, when $f = 5000$ Hz, the location of the vortexes are not far from the throat. The effective regions of the tubes in converging direction are smaller. The efficiency higher than that of $f = 1000$ Hz (refer to Fig. 10).

5.2.3 The influence of the volume change rate on efficiency

As shown in Fig. 17, when $\theta = 10°$ and $w_{max} \times f = 500$, the transient Reynolds number is about 740. There is no boundary layer separation in the tube. With the increase in volume change rate, as $w_{max} \times f = 800$, the transient Reynolds number is about 1150, the flow regime is jet flow in the middle of the tube and the effective diffusion region decreases. The vortexes consume the energy of the main flow, which result in the reduction of efficiency. When $\theta = 60°$, the flow regime is jet flow at the pump stage. With an increase in volume change rate, the width of the jet flow decreases, namely, the effective diffusion region decreases. As $w_{max} \times f = 500$, the width of the jet flow at the end of the tube is 48.84 % wider than that of $w_{max} \times f = 800$. Hence, the efficiency of the micropump decreases slightly with a rise in volume change rate when $f \leq 1000$ Hz.

The distributions of the velocity in the outlet tubes as $w_{max} \times f = 500$ and $w_{max} \times f = 800$ are shown in Fig. 18.

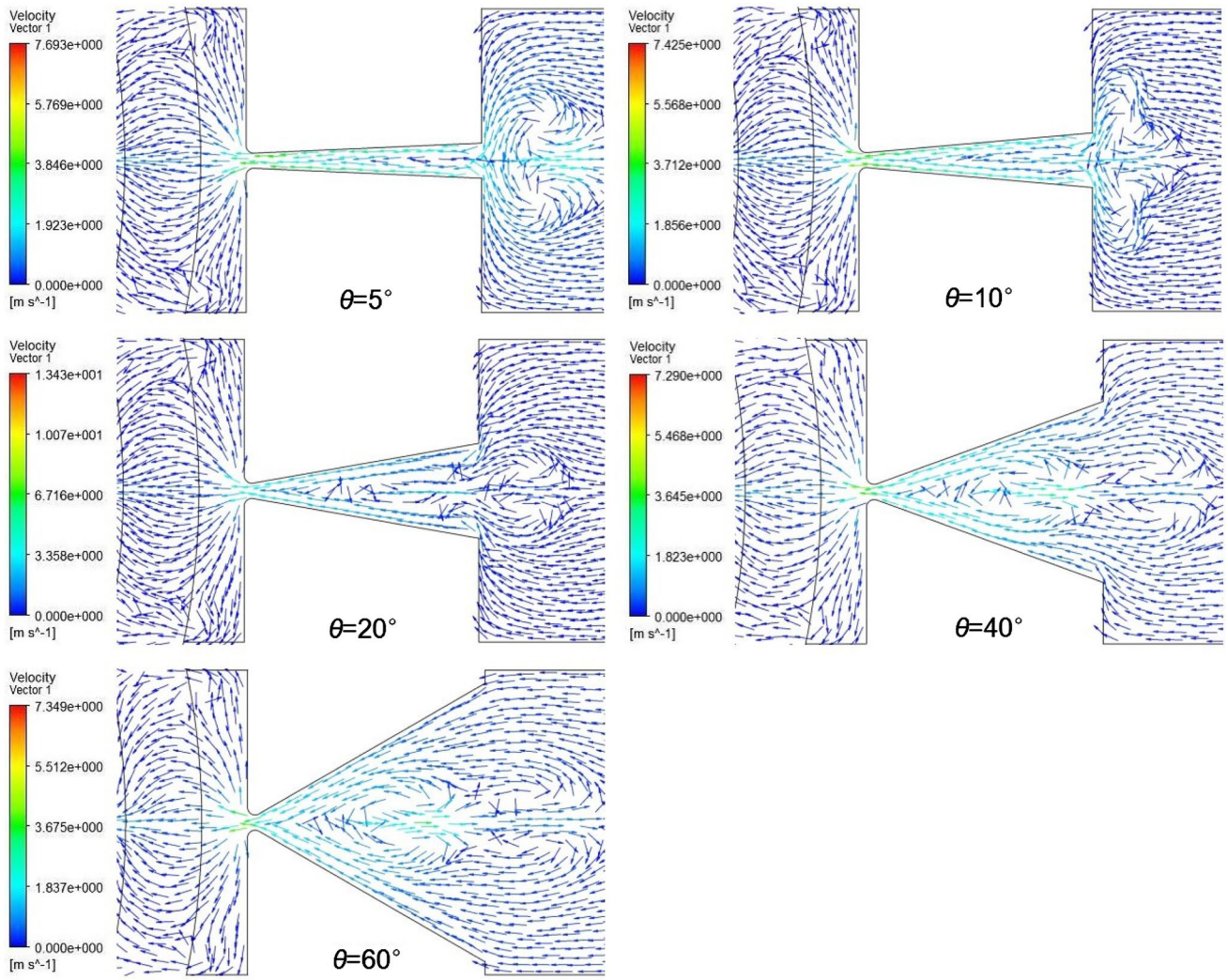

Fig. 15 The distributions of the velocity in outlet tube with different angles when $f = 1000$ Hz, $t = 0.86T$

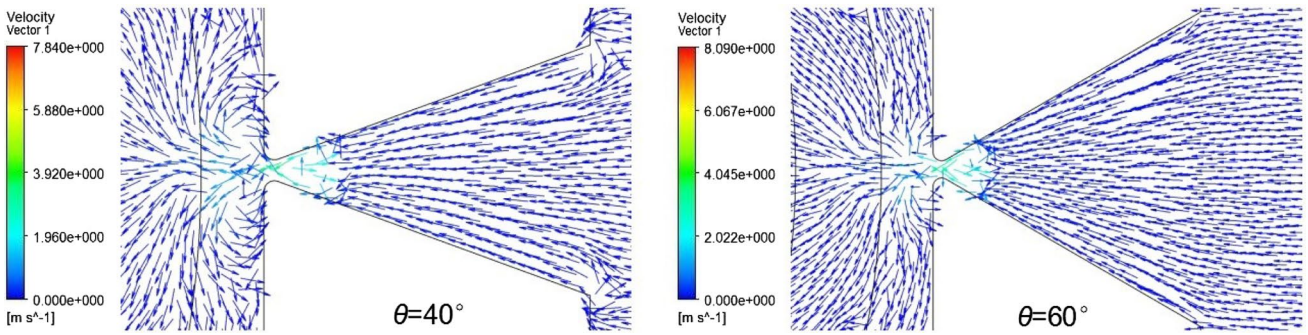

Fig. 16 The distributions of the velocity in the outlet tubes when $t = 0.8T$

As presented, when $f = 5000$ Hz, the vortexes expand during the deceleration suction stage because of the phase difference between flow rate and pressure. The relative pressure in pump chamber is positive (refer to 5.2.4), the adverse pressure gradient accelerates the development of the vortexes. As an increase in volume change rate, the pressure in pump chamber increases. As $\theta = 10°$ and $w_{\max} \times f = 500$, the vortexes expand at 0.15 T. It

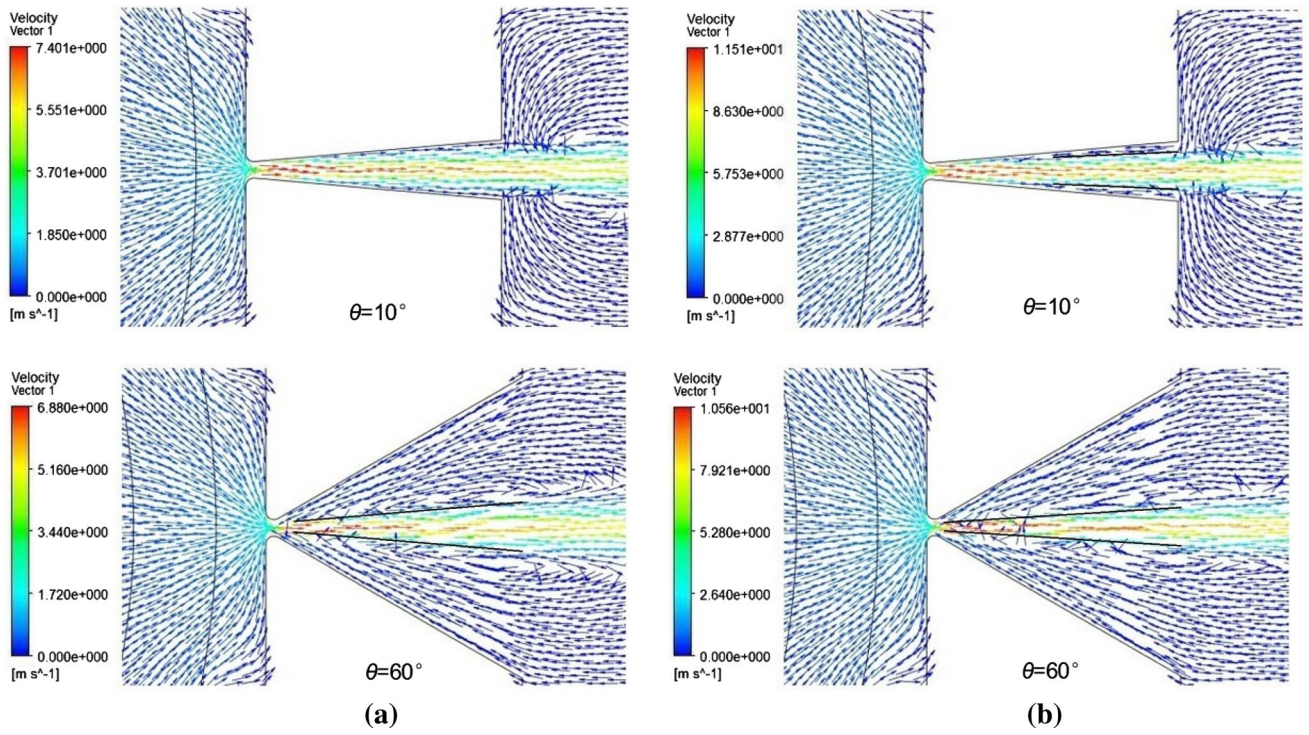

Fig. 17 The distribution of the velocity under $\theta = 10°$, $\theta = 60°$, $f = 10$ Hz when $t = 0.48T$. **a** $W_{max} \times f = 500$. **b** $W_{max} \times f = 800$

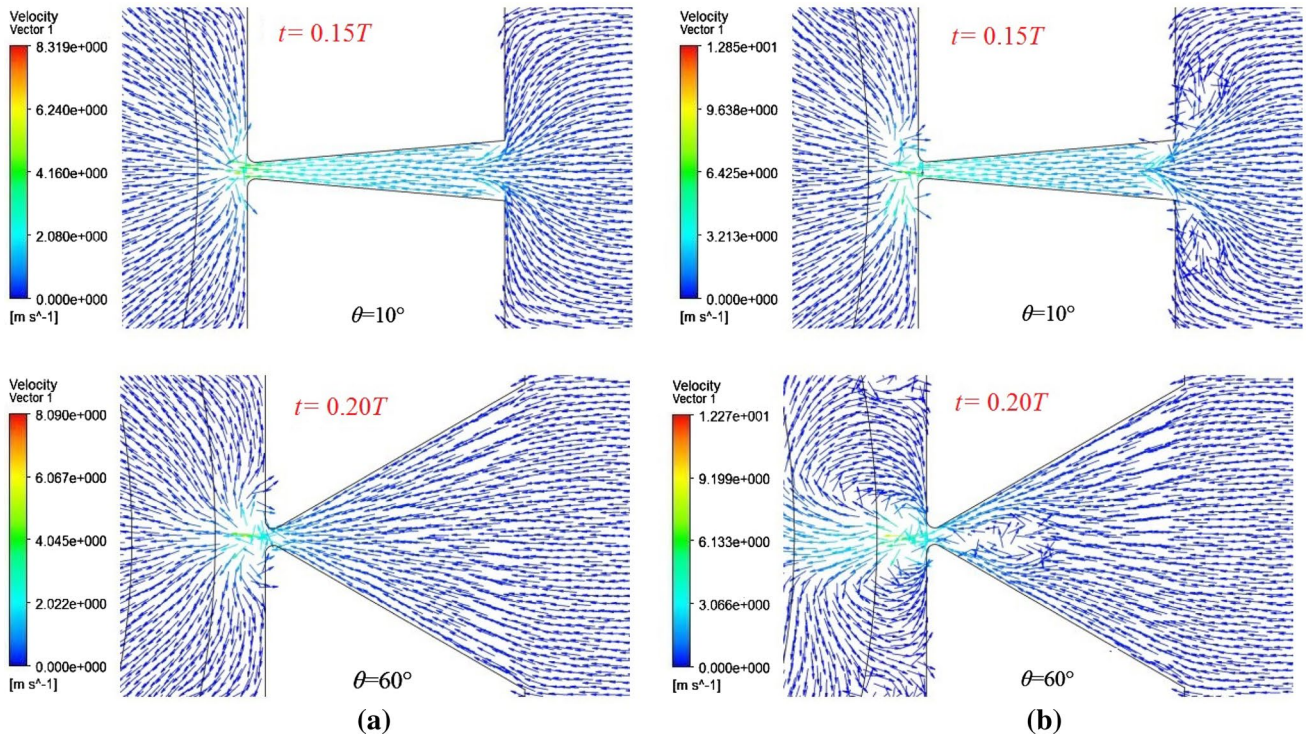

Fig. 18 The distributions of the velocity at the outlet tubes when $f = 5000$ Hz. **a** $W_{max} \times f = 500$. **b** $W_{max} \times f = 800$

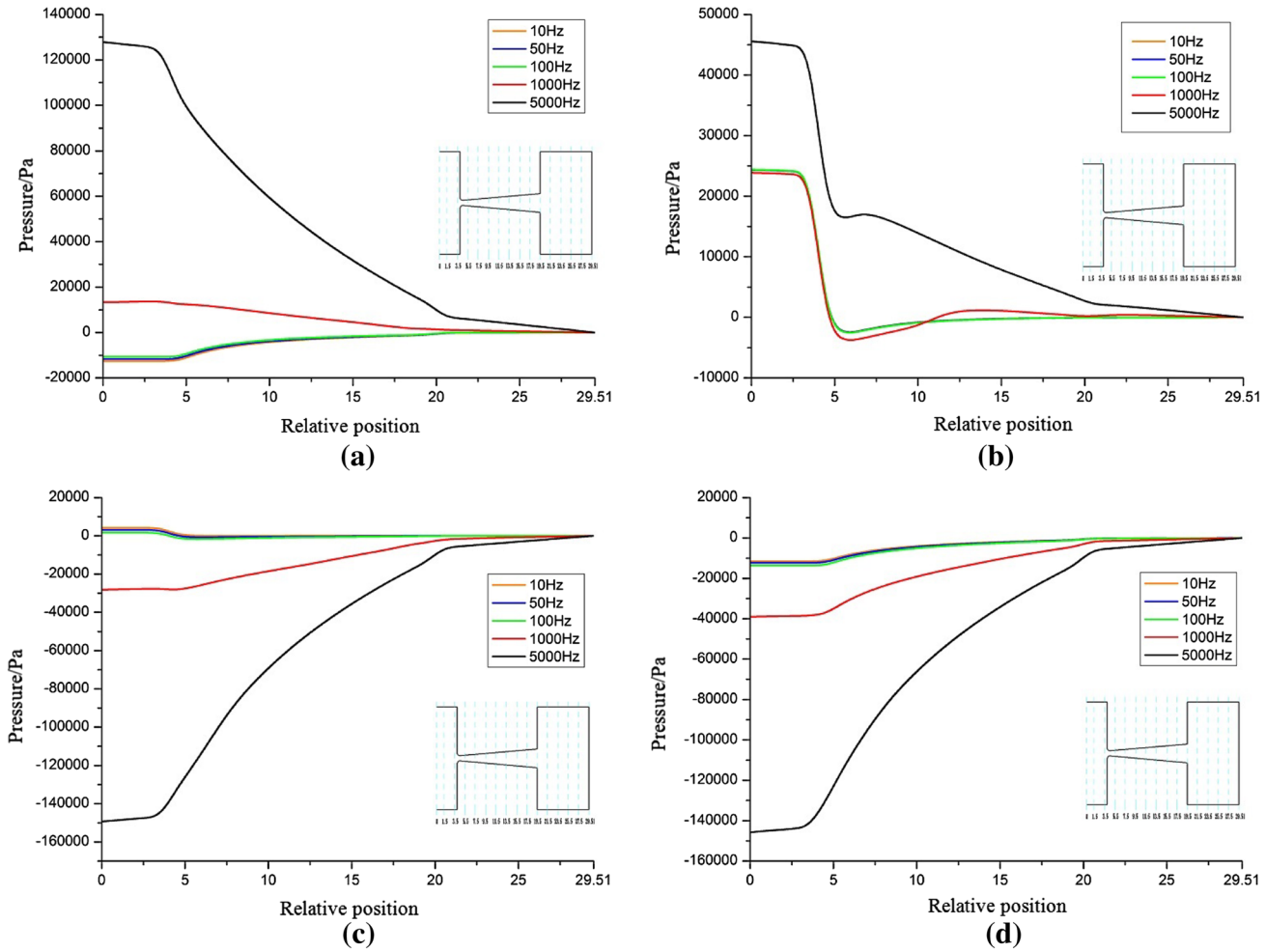

Fig. 19 The distributions of the pressure in the outlet tube at different frequency when $\theta = 10°$. **a** At 0.14 *T*. **b** At 0.5 *T*. **c** At 0.7 *T*. **d** at 0.86 *T*

would be 0.08 *T* as $w_{max} \times f = 800$, almost half the time in advance. As $\theta = 60°$ and $w_{max} \times f = 500$, there is no boundary layer separation. As $w_{max} \times f = 800$, the vortex occurs in the front of the tube at $t = 0.17T$ because of an increase in adverse pressure gradient. Therefore, the efficiency increases with an increase in volume change rate at $f = 5000$ Hz due to the vortexes at the deceleration suction stage.

5.2.4 The analysis of the pressure

The distributions of the pressure along the outlet tube are shown in Fig. 19. The left side of the buffer chamber is designated as origin and the relative position X is defined as the ratio of absolute position to throat width. In Fig. 19a, as $f \leq 100$ Hz, the relative pressure in pump chamber is negative, so the flow resistance is relatively small; when $f \geq 1000$ Hz, the relative pressure in pump chamber is positive due to the phase difference between the pressure and the flow rate (He and Cai 2014). The pressure gradient is opposite to the flow direction, the fluid sucked into the pump chamber decreases. When $f = 1000$ Hz, the positive pressure in the pump chamber accelerates the development the vortexes at the end of the tube. As shown in Fig. 19 (b), when $f = 1000$ Hz, the distribution of the pressure in the tube is similar to that at the low frequency, it proves that the flow regimes are similar during acceleration pump stage. As shown in Fig. 19c, when $f = 1000$ Hz, the relative pressure in pump chamber is negative. The boundary layer separates in advance due to the adverse pressure gradient, then the boundary layer separation point moves to the throat gradually, the boundary layer separation region develops very well. When $f = 5000$ Hz, the boundary layer separation point would be kept near the throat because of the overlarge adverse pressure gradient, the development of boundary layer separation region is restricted. As shown in Fig. 19d, compared with the cases at the low frequency, the pressure loss is greater when $f = 1000$ Hz, which proves that the vortexes consume energy at the acceleration suction stage. The tube

is partially blocked in converging direction and the efficiency increases.

6 Conclusions

1. The displacement of the membrane is measured by experiment, the results agree with the deformation model of the membrane very well. The volume change of pump chamber in a circle increases linearly with an increase in voltage.
2. The efficiency is almost independent of the frequency as $f \leq 100$ Hz; the efficiency increases with an increase in frequency as 100 Hz $\leq f \leq 1000$ Hz. The efficiency decreases with an increase in frequency as $f \geq 1000$ Hz and $\theta \leq 20°$. On the contrary, the efficiency increases with an increase in frequency as $f \geq 1000$ Hz and $\theta \geq 40°$. The optimal angle is 10° as $f \leq 1000$ Hz. The efficiency decreases with an increase in pump chamber volume change rate as $f \leq 1000$ Hz; however, the efficiency increases with an increase in pump chamber volume change rate as $f = 5000$ Hz.
3. The effective diffusion region is used to explain the effect of the diverging angle on the efficiency. The diverging flow is restricted by the walls as $\theta \leq 10°$. With an increase in diverging angles, the effective diffusion region increases. The efficiency is dictated by the diverging flow. As $\theta \geq 20°$, the flow regime is jet flow, the effective diffusion region is almost invariant as the pump chamber volume change rate is fixed. The efficiency depends on the converging flow.
4. The relationships among the efficiency, the frequency and the characteristics of the vortexes are revealed. The efficiency increases due to the existence of the vortexes in the tube at the suction stage as 100 Hz $\leq f \leq 1000$ Hz. As 1000 Hz $\leq f \leq 5000$ Hz and $\theta \leq 20°$, there is no boundary layer separation in the tubes, the efficiency decreases. As 1000 Hz $\leq f \leq 5000$ Hz and $\theta \geq 40°$, the vortexes appear in the front of the tube, the efficiency increases.
5. The micropump efficiency decreases with an increase in volume change rate when $f \leq 1000$ Hz. The flow regime is jet flow at the end of the tube, the flow resistance increases in diverging direction. Nevertheless, the tendency is opposite when $f = 5000$ Hz. The efficiency increases due to the vortexes caused by the great adverse pressure gradient.

In further work, the real flow field in miropumps should be obtained by Micro-PIV (Micro Particle Image Velocimetry). The quantitative relationship between the efficiency and frequency is expected by mathematics modeling. In addition, optimization methods (such as response surface method, orthogonal array table method) would be employed to get the optimal parameters.

Acknowledgments This work was supported by the project of the National Natural Science Foundation of China [Grant Number: 51276082]. Departments of Education and Finance, Jiangsu Province of P.R. China (A Project Funded by the Priority Academic Program Development of Jiangsu Higher Education institutions, PAPD) [Grant Number: SUZHENGBANFA (2014) No. 37].

References

Ahn CH, Allen MG (1995) Fluid micropumps based on rotary magnetic actuators. In: Proceedings of IEEE micro electro mechanical systems (MEMS), Amsterdam, Netherlands, pp 408–412

Andersson H, Wijngaart W (2001) A valve-less diffuser micropump for microfluidic analytical systems. Sens Actuators B 72:259–265

Aravind T, Kumar SP (2013) A novel thermopneumatic based micropump and microvalve using phase change liquid. 2013 International conference on smart structures and systems (JCSSS-20 13), Chennai, India, pp 66–69

Azarbadegan A, Eames I (2011) Computational study of parallel valveless micropumps. Sens Actuators B 158:432–440

Bodén R (2006) A polymeric paraffin actuated high-pressure micropump. Sens Actuators A 127:88–93

Bu M, Tracy M, Graham E (2003) Design and theoretical evaluation of a novel microfluidic device to be used for PCR. J Micromech Microeng 13:S125–S130

Cheng P, Wu HY (2007) Phase-change heat transfer in microsystems. J Heat Transf 129:101–107

Dewa AS, Deng K, Ritter DC, Bonham C (1997) Development of LIGA-fabricated, self-priming, inline gear pumps. Transducers'97, Chicago, pp 757–760

Gravesen P, Branebjerg J (1993) Microfluidics: a review. J Micromech Microeng 3:168–182

Guan YF, Zhang GX, Ren JC (2009) Fabrication and experiment studies of the piezoelectric micropump with saw-tooth microchannel. In: Proceedings-2009 IEEE international conference on intelligent computing and intelligent systems 2, pp 733–737

He XH, Cai SC (2014) Transient characteristics of flat-wall diffuser/nozzle elements of valveless piezoelectric micropumps. J Xi'An Jiaotong Univ 48(5):89–95

Hsu YC, Le NB (2009) Equivalent electrical network for performance characterization of piezoelectric peristaltic micropump. Microfluid Nanofluid 7:237–248

Izzo I, Accoto D, Menciassi A, Schmitt L, Dario P (2007) Modeling and experimental validation of a piezoelectric micropump with novel no-moving-part valves. Sens Actuators A 133:128–140

Jiang XN, Zhou ZY (1998) Micronozzle/diffuser flow and its application in micro valveless pumps. Sens Actuators A 70:81–87

Kuo CT, Liu CH (2009) A bubble-free AC electrokinetic micropump using the asymmetric capacitance-modulated microelectrode array for microfluidic flow control. J Microelectromech Syst 18(1):38–51

Lu F, Xie LY (2005) Investigation and application on micropump. Fluid Mach 33(6):29–34

Menter FR, Kuntz M, Langtry R (2003) Ten years of industrial experience with the SST turbulence model. In: Proceedings of the 4th international symposium on turbulence, heat and mass transfer, Antalya, Turkey, 12–17 October, 2003, pp 625–663

Nguyen NT, Huang X, Chuan TK (2002) MEMS-micropumps: a review. Trans ASME J Fluids Eng 124:384–392

Olsson A, Stemme G (2000) Numerical and experimental studies of flat-walled diffuser elements for valve-less micropumps. Sens Actuators 84:165–175

Olsson A, Stemme G, Stemme E (1995) A valve-less planar fluid pump with two pump chambers. Sens Actuators A 47:549–556

Peng XF, Peterson GP, Wang BX (1994) Frictional flow characteristics of water flowing through rectangular microchannels. Exp Heat Transf 7:249–264

Singhal V, Garimella SV (2004) Low Reynolds number flow through nozzle-diffuser elements in valveless micropumps. Sens Actuators A 113:226–235

Singhal V, Garimella SV, Raman A (2004) Microscale pumping technologies for microchannel cooling systems. Appl Mech Rev 57(3):191–221

Yang S, Yuan SQ, Cai SC, Wei DD, He XH (2014) A valveless piezoelectric micropump based on Coanda effect. Trans Chin Soc Agric Mach 45:343–348

Spencer WJ (1978) An electronically controlled piezo-electric insulin pump and valves. IEEE Trans Sonics Ultrason 25(3):153–156

Stemme E, Stemme G (1993) A valveless diffuser/nozzle fluid pump. Sens Actuators A 39:159–167

Su YF, Chen WY (2006) Electro-magnetically actuated valveless micropump with two flexible diaphragms. Int J Adv Manuf Technol 30:215–220

Tanaka S, Tsukamoto H (2008) Development of diffuser/nozzle based valveless micropump. J Fluid Sci Technol 3(8):999–1007

Wang CT, Chen YM (2014) Tesla valves in micromixers. Int J Chem React Eng 12(1):397–403

Wang YC, Hsu JC (2009) Loss characteristics and flow rectification property of diffuser valves for micropump applications. Int J Heat Mass Transf 52:328–336

Wang XY, Cheng C (2009) Electroosmotic pumps and their applications in microfluidic systems. Microfluid Nanofluid 6:145–162

Yuan SQ, Yang S (2015) Design and experimental study of a novel three-way diffuser/nozzle elements employed in valveless piezoelectric micropumps. J Braz Soc Mech Sci Eng 37:221–230

Zhang T, Wang QM (2005) Valveless piezoelectric micropump for fuel delivery in direct methanol fuel cell (DMFC) devices. J Power Sources 140:72–80